

# Image Quality of the Helioseismic and Magnetic Imager

R. Wachter<sup>1</sup>, J. Schou<sup>1</sup>,  
M. C. Rabello-Soares<sup>1</sup>, J. W. Miles<sup>2,3</sup>,  
T. L. Duvall Jr.<sup>4</sup> and R. I. Bush<sup>1</sup>

© Springer ●●●

**Abstract** In this paper, we describe the imaging quality of the Helioseismic and Magnetic Imager (HMI) onboard the Solar Dynamic Observatory (SDO) as it was measured during the ground calibration of the instrument. We describe the calibration techniques and report our results for the final configuration of the instrument. We present the distortion, Modulation Transfer Function, stray light, image shifts introduced by moving parts of the instrument, best focus and field curvature, and the relative alignment of the two cameras. We investigate the gain and linearity of the cameras, and present the measured flat field.

**Keywords:** Helioseismology, Observations; Instrumental Effects; Solar Dynamics Observatory

## 1. Introduction

The Helioseismic and Magnetic Imager is a 14cm aperture imaging Solar instrument with an effective focal ratio of 37.4. It is built to operate in monochromatic light at 6173 Å. The spectral filters are realized by the front window, a wide band blocker filter, a tunable five element Lyot filter, and two Michelson interferometers. The images are stabilized against spacecraft jitter by an Image Stabilization System (ISS) and the images are recorded by two cameras, both equipped with a 4096<sup>2</sup> pixel CCD. Two adjustable legs at the HMI Instrument allow a correction of longterm alignment drift of the Instrument versus the SDO satellite. Focus adjustment is achieved by placing a pair of fused silica plane parallel plates into the optical path. Two focus wheel with five openings, each with 3 plates of varying thickness, an open position, and a lens, which is used to

---

<sup>1</sup> Stanford University, Stanford, CA, 94305 email: richard@sun.stanford.edu

<sup>2</sup> Lockheed Martin Advanced Technology Ctr., Palo Alto, CA, 94304

<sup>3</sup> SOFIA-USRA, NASA Ames Research Center MS N211-3, Moffett Field, CA 94035, USA <sup>4</sup> Solar Physics Laboratory, NASA/Goddard Space Flight Center, Greenbelt, MD 20771, USA

image the aperture for calibration purposes, provide 16 discrete focus positions. For a detailed description of the optical design of the Instrument, see Schou *et al.* (2010).

The optical calibration of the Instrument aims at optimizing and characterizing the Instrument in a way that allows us to calculate observables from the raw data (filtergrams) which are free of avoidable instrumental artifact. The observables, the most important being magnetic fields and Doppler velocities, are fed into a data processing pipeline that resolves the surface and subsurface structure of the Sun (see Couvidat *et al.* (2010)).

The instrumental effects that can be corrected for in the observables calibration need to be known as accurately as possible, whereas the instrumental influences which can not be corrected for need to be sufficiently small to meet the accuracy requirements for the observables. Among the instrumental artifacts that can be corrected for in the observable calibration is the flat field (detector and optical), the distortion, the relative alignment of the two cameras, and the residual image motion caused by movable parts in the Instrument. A suboptimal Modulation Transfer Function (MTF), and a field tilt or curvature can not easily be corrected for and therefore these optical characteristics need to strictly meet the specifications in order to obtain observables with the required accuracy. The first group of instrumental artifacts needs to be characterized with sufficient accuracy, while the second group requires both optimization and characterization. Scientific modeling of the data often requires a good knowledge of any residual instrumental artifacts.

The calibration efforts were therefore focused on:

1. bringing the point spread function close to the optimum set by the diffraction limit and measuring the remaining optical aberrations. The stray light, which is the tail of the point spread function, is measured separately.
2. measuring the distortion as accurately as possible.
3. setting the best focus in the middle of the available focal range for both cameras.
4. minimizing and characterizing field curvature and tilt.
5. measuring the misalignment of the cameras as accurately as possible.
6. minimizing the image motion introduced by the moving parts of the Instrument, and obtaining a consistent picture of the remaining movements.
7. measuring the non-linearity of the camera response to light exposure, and verifying the saturation level.
8. measuring the gain of the detector amplifiers
9. measuring the flatfield on all scales, and monitoring its change in different environments.

We note that the above mentioned characterizations can be repeated after launch, although certain tests have to be done in a different way. In some cases, more accurate numbers are expected from the space measurements and will be made available as soon as possible. A detailed presentation of our results from the ground measurement and its later comparison with the in flight measurements will show both the temporal drifts of the Instrument and any effects of the launch. It will also be instructional for future calibrations of imaging space instruments.

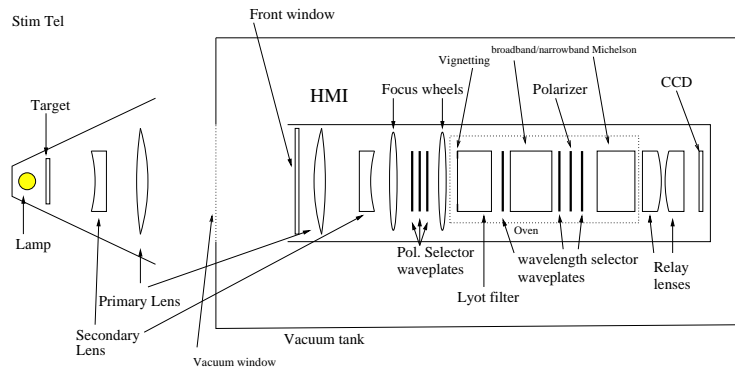


**Figure 1.** A cartoon of the calibration measurement setup. The Instrument is highly simplified, with only the elements most relevant for the image quality shown.

## 2. Calibration Setup

### 2.1. Instrument and Stimulus Telescope

All image quality calibration measurements are performed with a Stimulus Telescope projecting a target into the Instrument. The Stimulus Telescope is identical to the telescope part of the Instrument in reversed direction (primary and secondary lens, no front window) with the illuminated target mounted in the focal plane of the stimulus telescope. The target is illuminated by a lamp, providing a source of white light. The rays originating from the target are refracted by the secondary and primary lens of the Stimulus Telescope, and a collimated beam exits the Stimulus Telescope, mimicking an object at infinite distance observed by the Instrument. The optical axis of the Stimulus Telescope and the Instrument are aligned (except for measurements where a controlled misalignment is required). With the help of the Stimulus Telescope, a target at a finite distance can be imaged by an instrument which is built to image an object at infinite distance (the Sun).

The system consisting of the Stimulus Telescope and the Instrument is generally subject to thermal and vibrational perturbations in its environment. While the Instrument has thermal control through various heaters and sensors at the Instrument (with the spectral filters being placed in the thermally controlled oven), the Stimulus Telescope has no such control. Instrument and Stimulus Telescope were stabilized against vibrational perturbations using a floating table. Blurring from turbulent air currents in the optical path turned out to be the major source of high frequency noise in the image quality measurement.

Most of the time, the Instrument is subject to the same environment as the Stimulus Telescope (“in air measurements”). However, the Instrument is occasionally placed in a vacuum tank in order to test the Instrument at temperatures that resemble space condition. In particular, the dark current in the CCD detectors is drastically reduced, because the CCDs operate at much lower temperatures. In this setup, a glass window in the wall of the vacuum tank is intercepting the collimated beam between the Stimulus Telescope and the

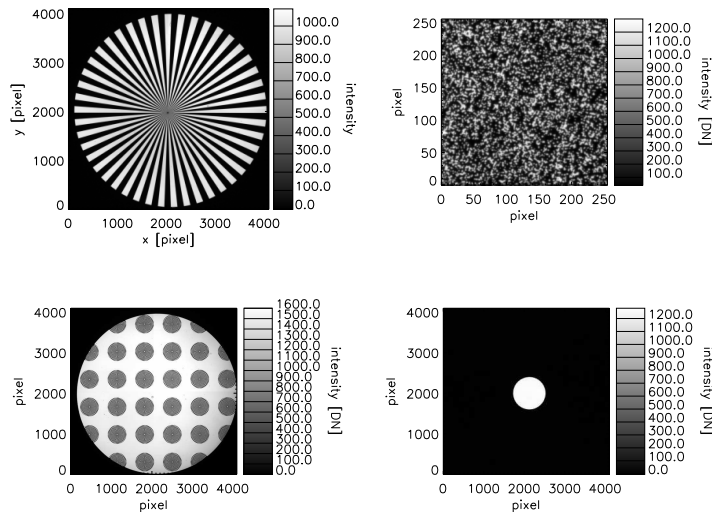


**Figure 2.** Focused instrumental images of different targets: the star target (upper left), the random dot target (upper right), the star array target (lower left), and the 5 mm field stop (lower, right).

Instrument. This window is an additional uncontrolled element in the optical path of the system, introducing a temperature dependent amount of optical power (and possible other aberrations) into the system.

Figure 1 shows a very simplified layout of the calibration setup. It only shows the optical elements of the Instrument that are most important for the image quality. For a detailed optical prescription of the Instrument, see Schou *et al.* (2010) in this volume.

## 2.2. Test Facilities

The tests have been carried out at the Lockheed Martin Advanced Technology Center (LMSAL) in Palo Alto before November 2007, at the Goddard Space Flight Center (GSFC) between 11/2007 and 07/2009, and at the Astrotech Facilities in Titusville, Florida (ASO) until launch. The results from each series of measurements reflect the different thermal and vibrational perturbations of the environment. Also, the orientation of the Stimulus Telescope with respect to the Instrument at LMSAL is 90 degree different from the other two facilities. The Instrument has been put into the vacuum tank twice, but only the first time it was possible to put light into the Instrument.

## 2.3. Targets

The most common Stimulus Telescope targets used for imaging are shown in Figure 2. They are described below:

1. The random dot target:

A distribution of randomly placed dots of different diameters. The target is made to provide a strong signal on all spatial scales. It is non-repetitive (except for very large distances), so that displacements can be measured uniquely and accurately. This is important for camera alignment and distortion measurements. The target is isotropic and has a translationally invariant power spectrum, which means that the relative MTF can be measured with the random dot target at any position and in any spatial direction. Therefore, the best focus and the field curvature and tilt can be best measured with the random dot target.

2. The star target:

It consists of a star with triangular rays of light and shadow. A star target is created to perform absolute measurements of the MTF. The response at single frequencies can be inferred from the different radial distances from the center. However, the different frequencies are measured at different field positions.

3. The star array target:

Same as the star target, but with multiple, smaller stars covering the optical field. While the very low spatial frequencies are not available, the star array target examines the variation of the MTF across the field of view.

4. The field stop target:

A round field stop, limiting the field of view by some amount. We use field stops in a range from 5 mm to 27.4 mm, which are very close to the edge of the field of view. Large field stops provide guidance about the alignment of the stimulus telescope and the Instrument, while they introduce no signal for the HMI nominal field of view.

## 2.4. Light Sources

For most of the tests, we used an intensity stabilized lamp, which feeds an optical fiber. The exit of the optical fiber is projected onto the aperture of the stimulus telescope.

Another light source is a Light Emitting Diode (LED) which sits behind the beam splitter in front of the cameras. The light is not transmitted through large parts of the Instrument's optics. In particular, it is not spectrally filtered, and the LED wavelength is different from the HMI target wavelength. With the LED, images can be taken even if it is technically not possible to feed light into the Instrument. In this paper, only the gain and linearity tests use data obtained with the LED.

## 3. MTF

### 3.1. Direct Measurement

The MTF can be measured directly by using a star target (see Figure 2). Each radial distance from the star center can be associated with a single spatial frequency. The star is remapped in polar coordinates, and a sine wave is fitted

for each radial distance. The square wave to sine wave transformation results in a constant factor, and the pixel integration results in a *sinc* function factor. The azimuthal variation of the star target image reveals the directional dependence of the MTF, which is dominated by the astigmatism of the imaging system.

The star array target (see Figure 2) provides information about the large scale spatial variation of the MTF.

The MTF can also be derived from the images of the random dot target by dividing out the power spectrum of the target.

Using the setup consisting of Stimulus Telescope and Instrument, the wavefront error due to the Stimulus Telescope and Instrument can not be disentangled. To obtain the MTF of the Instrument itself, the interferometric measurement of the aberrations in the Stimulus Telescope need to be subtracted from the the measurement of the aberrations of the combined system (see Section 3.3).

We observed fluctuations in the measured MTF on small time scales, leading to a variation in the Strehl ratio of several percent. The magnitude of the fluctuation depend on the particular environment in which the measurements have been obtained. Both jitter and air currents can be responsible for the random blurring on small time scales, while thermal degradation take effect on longer time scales. We conclude that air currents, rather than jitter, are the major source of noise, because the ISS is taking out most of the environmental jitter effectively. To take out the residual jitter, we placed the Instrument and the Stimulus Telescope on a floating table. We didn't observe substantial improvements.

The test facilities at GSFC didn't provide a stable room temperature, which caused the aberrations to vary with time, and, at the same time, degrade the MTF. In a thermally stable environment, the measured Strehl ratio could be consistently determined at  $0.74 \pm 0.03$  (see Figure 4). We define the Strehl ratio here as the peak intensity of the combined system of Instrument and Stimulus Telescope divided by the peak intensity for the system as designed<sup>1</sup>.

Strehl ratios above 0.8 have been measured. As we have no indications that the Stimulus Telescope is canceling out large parts of the wavefront errors of the Instrument, we expect that the Strehl ratio of the Instrument will be in general at the upper end of all the measured values. Thermal perturbations and air currents in general degrade the MTF.

Our initial MTF measurements revealed a severe degradation of the MTF caused by the front window. We suspect that internal tensions caused by the layered front window design introduced large wave front errors at the entrance pupil. As a remedy, the surface of the front window was polished to compensate for the internal wave front error. Additionally, the known astigmatism of the telescope part of the Instrument has been taken out by the front window. The procedure resulted in a dramatic improvement of the MTF. Apart from the MTF variations caused by temperature gradients, we have not seen a degradation of the MTF over time.

---

<sup>1</sup>The Strehl ratio of the system as designed is 0.980, whereas the Strehl ratio of the Instrument as designed is 0.996. These numbers are relative to their respective diffraction limit.

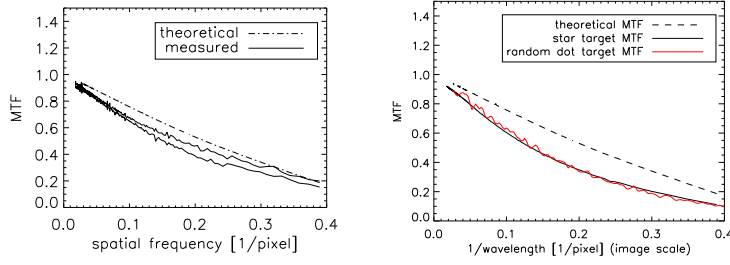


**Figure 3.** *Left panel:* The MTF measured with the star target. The theoretical curve represents the system of Stimulus Telescope and the Instrument together. The two solid curves represent the MTF in the two perpendicular directions with the maximum and the minimum amplitude. *Right panel:* The azimuthally averaged MTF together with the random dot target (red line), and measured with the star target (black line). The MTF can be inferred from the image of the random dot target by dividing out the known power spectrum of the target.

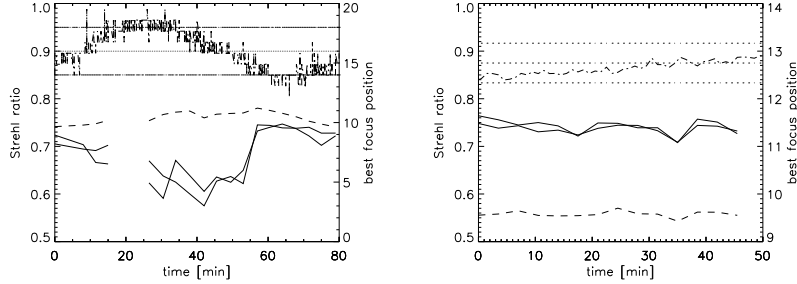


**Figure 4.** *Left panel:* Strehl ratio at best focus measured from a series of focus sweeps on a random dot target in the test facilities of Goddard Space Flight Center in September 2008. The dashed curve gives the variation of the best focus. The upper curve shows the room temperature, with the three dotted lines representing 20.7, 20.8, and 20.9 °C. *Right panel:* The same quantities as in the left panel, measured in the test facilities of Astrotech in August 2009. The horizontal lines represent 23.6, 23.7, and 23.8 °C.

Figure 3 provides an estimate for the MTF of the combined system, comparing it to the function expected for a perfect Instrument and Stimulus Telescope. This MTF represents a circular area of radius 400 pixels at the center of the image. As we have a clearly measurable amount of astigmatism in the system, we show the MTF in the two directions with maximum and minimum blur. For all other directions, the MTF will be in between these two lines.

### 3.2. Field Variations of MTF

For the variation of the MTF across the field, we need to assume that the target and the turbulent disturbances are homogeneous across the field. The star array target shows a MTF that has a higher Strehl ratio off a diagonal from the upper left to the lower right corner of the CCD. Figure 5 shows the Strehl ratio measured for the central 16 stars (see Figure 2) of the star array target.

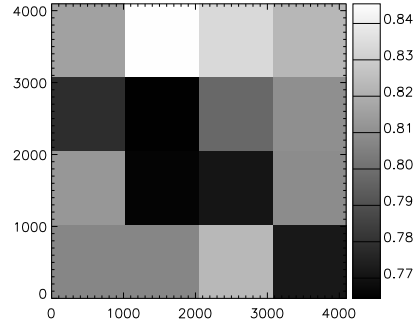


**Figure 5.** Strehl ratio as a function of field position measured with the star array target.

### 3.3. Phase Diversity Measurements

In order to further characterize the optical imperfections we also performed a phase diversity analysis. To this end focus sweeps of the random dot target were used. Cross spectra of a reference image near best focus and images at adjacent focus positions were calculated on  $128 \times 128$  patches which were then averaged over 16 patches near the center of the image in order to improve the signal to noise ratio. A model of the cross spectra was then fitted to the observed spectra while marginalizing over the power spectrum of the target.

The phase diversity analysis reveal several interesting results. The consistently most significant term is a spherical aberration of order  $-0.12$  waves. The interferometry of the Stimulus Telescope indicates that it contributes about  $-0.02$  waves and that the Instrument thus has  $-0.10$  waves, substantially more than the as designed value of  $-0.01$  waves.

The other terms are somewhat smaller than this. Unfortunately it has proved difficult to correct them for the effects of the stimulus telescope, which was only measured at one occasion. If it is assumed that it is constant in time then a change in the various values should be seen between the system values determined with no roll at LMSAL and  $90$  degree roll at GSFC and ASO. Unfortunately, the values at GSFC and ASO are not in all cases consistent and the changes from LMSAL are not those expected from the Stimulus Telescope interferometry. A possible reason for this is that the Stimulus Telescope is not stable in time, because the mounts are not stress free.

We have also attempted to determine the Strehl values for the combined system from the phase diversity numbers. We found that while the numbers generally agree in magnitude, their variation does not agree with the variation estimated directly from the images. The cause of this is unclear, but may be related to non-uniformities in the Stimulus Telescope illumination.

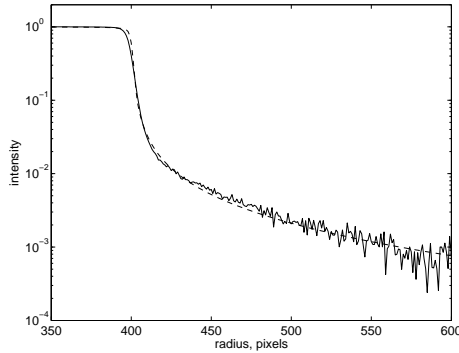


**Figure 6.** The azimuthal average intensity versus radial distance from the center of the field stop.

#### 4. Scattered Light

The instrumental scattered light can lead to important systematic effects, most importantly in the umbra of sunspots where the scattered light may be a significant fraction of the intensity (Bray and Loughhead (1979)). Properly characterized scattered light can be deconvolved, as was done by Jefferies and Duvall (1991) and Toner, Jefferies, and Duvall (1997).

To characterize the scattered light in the HMI instrument, a field stop of radius 400 pixels is imaged onto the CCD through the optical system. Ideally this would appear in intensity as a disk with zero intensity off the edge. In Figure 6, the azimuthally-averaged intensity is shown out to about 200 pixels from the edge, where it falls to  $10^{-3}$  of the disk intensity. Overplotted on the data is the result of a model calculation that we will now describe.

We would like to develop the point-spread function (PSF) of this instrument to include the scattering that leads to the extended tail in Figure 6. A simple empirical model of the PSF, with parameters describing a narrow core and an extended tail of the PSF, is given by Pierce and Slaughter (1977):

$$A(r) = (1 - \epsilon)e^{-(r/w)^2} + \frac{\epsilon}{1 + (r/W)^\kappa}, \quad (1)$$

where  $r$  is radial distance,  $\epsilon$  determines the relative sizes of the two parts,  $w$  is the width of the central Gaussian core,  $W$  is the width of the extended tail, and  $\kappa$  determines how fast the extended tail drops off. To determine a set of parameters that fits the observations, a disk of radius 400 pixels (which is a model for the field stop) is convolved with the model PSF. The parameters  $\epsilon = 0.1$ ,  $\kappa = 3.0$ ,  $w = 1.8$ , and  $W = 3.0$  provide the best fit. The result is plotted together with the data in Figure 6. While the overall fit is good, the small deviation near the edge can be attributed to the simplified representation of the core function as a Gaussian. Here however, we are mainly concerned with the extended tail.

Using this function, the scattered light can be removed by deconvolution in regions where it is important, such as the sunspot umbra.

## 5. Distortion

### 5.1. Distortion measurement

To measure the distortion, the random-dot target is mounted in the Stimulus Telescope. A set of images is taken at various alignment leg positions. Small areas of the images (256x256 pixels), corresponding to the same location on the target, but different positions in the optical field, are cross-correlated. The estimated shift between them corresponds to the difference in the leg position of the images plus the difference in the amount of distortion of the regions. This method of measuring distortion has the advantage that it does not depend on knowing the absolute properties of the Stimulus Telescope and the target. The distortion as a function of field position is expanded into Zernike polynomials. Zernike polynomials were chosen because they are orthogonal over a unit disk. The polynomials are normalized so that they form an orthonormal basis. The value at the CCD center is forced to zero, as well as the terms describing the image scale, the roll, and the ellipticity, because they are unconstrained by this method. Our model was fitted to the observed shifts using a non-linear least squares fit. The Zernike coefficients are estimated together with the errors in the nominal leg positions. This way, the obtained distortion does not depend on an exact knowledge of the displacement caused by offsetting the alignment legs. Several sets of images were taken from June 2007 to August 2009. We fitted the distortion for each of 29 sets. A Zernike polynomial of 23th order was found to be adequate, i.e. no significant improvement was found using a higher order.

### 5.2. Distortion results

To get a best estimate of the distortion, the fitted distortion at a given focus position and camera was averaged over all image sets. This best estimate of the distortion is shown at Figure 7 for the front camera near nominal best focus (focus nine). The distortion is smaller than two pixels at any field position.

We measure the magnitude of the residuals by

$$R_n = \sqrt{\sum_{\mathbf{r}} |\mathbf{D}_n(\mathbf{r}) - \mathbf{D}_n^f(\mathbf{r})|^2 / (2N_{\mathbf{r}})}, \quad (2)$$

where  $\mathbf{D}_n$  is the distortion vector measured at a particular set, and  $\mathbf{D}_n^f$  is the best fit for each of these measurements. We average over all  $N_{\mathbf{r}}$  points in the spatial grid. This number represents the error of individual measurements. The mean over  $R_n$  and its standard deviation is  $0.043 \pm 0.005$  pixels for the front camera and  $0.044 \pm 0.005$  pixels for the side camera near best focus. This number increases away from best focus, because shifts obtained from cross correlations are less accurate for blurred images.

We compare this number with the deviation from the mean of all measurements:

$$S_n = \sqrt{\sum_{\mathbf{r}} |\mathbf{D}_n^f(\mathbf{r}) - \overline{\mathbf{D}^f(\mathbf{r})}|^2 / (2N_{\mathbf{r}})} \quad (3)$$

The mean and the standard deviation of  $S_n$  is  $0.057 \pm 0.027$  pixels for the front camera and  $0.050 \pm 0.026$  pixels for the side camera. This number increases to 0.10 pixel when the image is out of focus. This means that the changes seen over time are not significant beyond the two sigma level. A closer look at individual sets suggest that the variation is slightly increased when the temperature of the environment is unstable. This indicates that within the accuracy of our measurements, the distortion is only weakly sensitive to the different thermal environment in which the measurements have been taken, and remained constant throughout the integration of the Instrument into the satellite.

### 5.3. Variation of the distortion with camera

The mean difference between the distortion in the two cameras was calculated by averaging the difference between the fitted distortion for each camera over all sets at a given focus position. Figure 8 shows the mean difference between the two cameras at focus position nine (which is the nominal best focus of the Instrument). The difference is everywhere smaller than 0.28 pixels. The differences in the distortion in the horizontal direction are statistically significant ( $\approx 10$  sigma) and larger than in the vertical direction, which are barely significant ( $\approx 2$  sigma) - sigma is a standard deviation derived from the difference between the two cameras for different data sets. The additional distortion must be caused by a optical element behind the beamsplitter that separates the optical path of the two cameras, or by the CCD itself. We suspect the folding mirror to be responsible for the observed difference in the cameras.

### 5.4. On Orbit rolls and Offsets

The image scale will be measured in space by looking at the size of the solar disk. The roll can be determined from lunar transits.

The ellipticity terms can easily be measured on orbit by rolling the spacecraft around the spacecraft- Sun axis and measuring the changing shape of the solar limb.

By a combination of rolls and offsets, it is also possible to determine further terms in the distortion by tracking the limb and supergranulation, as demonstrated with MDI (see Scherrer *et al.* (1995)). The plan is to do such calibrations on a regular but infrequent basis.

## 6. Focus and Camera Alignment

To determine the best focus position, we take an image of the random dot target at all available focus positions (“focus sweep”) and look for the maximum spatial power at intermediate frequencies, where the power depends most strongly on

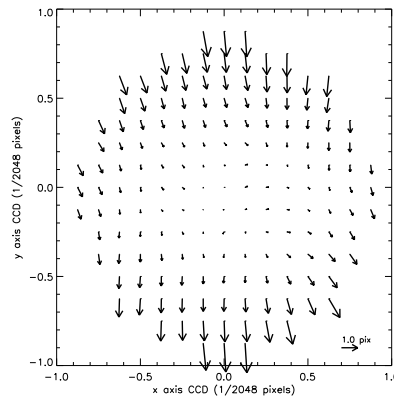


**Figure 7.** Estimated distortion near best focus for the front camera.

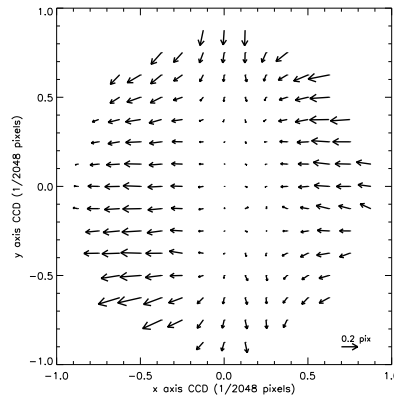


**Figure 8.** Difference between the distortion of the front camera and the side camera for focus position 9. The difference has been obtained as an average from all available sets of measurements.

focus (between 13% and 28% of the pixel Nyquist frequency). Fitting a quadratic function to the average power as a function of focus position allows us to determine the best focus in fractions of focus steps. The random blur introduced by air currents limits the accuracy of single measurements of the best focus to 0.1 focus steps.

As the setup of the Stimulus Telescope tries to achieve a nearly collimated beam entering into the Instrument, focusing on the target is equivalent to focusing on the Sun. An air to vacuum corrector in front of the Instrument corrects for the fact that there is air in the Instrument. We aim at a best focus in the middle of the available focus from position one through sixteen. The best focus of the two cameras should not differ by more than 0.5 focus steps. Table 1 (right columns) gives the focus of both cameras for different measurements. Focus position 9 is just above the middle of the available focus range, and is the nominal best focus of the Instrument. We aimed at bringing the best focus of the Instrument

**Table 1.** Relative lateral shift between the two cameras ( $x,y$ ), the relative rotation ( $rot$ ) in degrees, and the best focus position (range: 1 – 16) for the front and side camera for different measurements during the calibration campaign.

Date	x	y	rot	Focus front	Focus side
02-18-2008	-6.6	5.5	0.082	10.9	10.9
02-14-2008	-6.4	5.7	0.081	9.7	9.4
01-30-2008	-6.2	5.3	0.082	8.2	8.2
11-03-2007	-6.1	4.3	0.079	10.4	10.3
11-02-2007	-6.2	4.3	0.080	9.9	9.7
10-28-2007	-6.7	3.5	0.080	8.8	8.7
10-14-2007	-4.5	4.5	0.082	9.1	9.1

slightly above the middle of the focus range, because the heaters at the front window are able to lower the best focus position, but not to raise it.

The measured focus of the Instrument shows some variation. We know that a temperature gradient across the front window introduces refracting power. As the gradient is controlled by the heaters at the rim holding the front window as well as the air temperature, a good control of the front window gradient is difficult to achieve in the absence of a strictly controlled room temperature. This is reflected in the fluctuating focus values. The focus difference between front and side camera, however, are well within the tolerance limits, with a marginally higher focus ( $\approx 0.2$  focus steps) for the front camera.

Note that the best focus can not be reliably measured when the Instrument is in the vacuum tank, as the window of the vacuum tank introduces unknown refracting power to the system.

Some of the proposed observables frame lists require us to combine the raw images of both cameras. To do so, the co-alignment of the cameras needs to be known accurately. The alignment of the cameras can be determined from simultaneous focus sweeps on both cameras by using cross-correlation techniques. We derived a relative lateral shift and a relative rotation for the images of the two cameras, and found the lateral shift to slightly drift over time scales of several month. The relative shifts and rotations are given in Table 1. The observed long-term changes are most likely caused by the changing mechanical stresses on the Instrument or the changing thermal environment. We will be able to measure the shifts very accurately in space and to monitor them continuously.

## 7. Field Curvature

Field curvature measurements use the same data sets as distortion measurements. Image offsets, using the alignment legs to vary the pointing, allow to distinguish between the properties of the Stimulus Telescope and the Instrument. The images in the front camera and the side camera were recorded alternately.

**Table 2.** Field tilt and curvature for the front and the side camera. The numbers represent the focus change in units of nominal focus steps from edge to edge for the focus gradient, and the change from center to edge for the quadratic focus term. The numbers have been derived from a series of twelve field curvature measurements in an unstable temperature environment at GSFC.

	grad x	grad y	quadratic
front cam. 06/2008	$0.01 \pm 0.15$	$-0.13 \pm 0.24$	$0.40 \pm 0.01$
side cam. 06/2008	$0.09 \pm 0.17$	$-0.45 \pm 0.20$	$0.41 \pm 0.01$

Using the random dot target, we measure the best focus as a function of field position,  $f(x, y)$ , and fit the model:

$$f(x, y) = a_H x + b_H y + c_H (x^2 + y^2) + a_S (x - x_L) + b_S (y - y_L) + c_S ((x - x_L)^2 + (y - y_L)^2) + d. \quad (4)$$

Here,  $x$  and  $y$  are coordinates of the HMI image and  $x_L$  and  $y_L$  are the image shifts introduced by offsetting the optical axis of the Instrument using the alignment legs.  $x_L$  and  $y_L$  can be measured by cross-correlating the images of the random-dot target.  $a_H$  and  $b_H$  measure the horizontal and vertical component of the HMI field tilt, and  $c_H$  measures the (quadratic) field curvature.  $a_S$ ,  $b_S$ , and  $c_S$  measure the respective quantities for the Stimulus Telescope. Using all 13 or 25 leg positions, the coefficients  $a_{H,S}$ ,  $b_{H,S}$ ,  $c_{H,S}$ ,  $d$  are overdetermined and can be obtained from a least square fit. Note that the constant focus term  $d$  can not distinguish between the Stimulus Telescope and the Instrument.

We found that while there is consistency in the inferred quadratic term, the linear gradient term fluctuates wildly.

Field curvature measurements at GSFC were performed in an unstable temperature environment, which leads to a focus changing with time. Figure 9 shows a measurement of the best focus together with a record of the outside temperature. It indicates that the focus position follows the temperature gradient with a time lag.

As the model described by Equation 4 assumes a focus independent of time, temporal variation of the focus lead to spurious field curvatures.

In order to understand the fluctuations of the measurements, we performed a series of 12 field curvature sequences with identical setup. Figure 10 shows the strong anti-correlation between the gradients measured for the Stimulus Telescope and the Instrument.

We simulated a sinusoidal focus drift with a period of 2.2 hours, and amplitude of 0.75 focus steps and a random phase. These parameters represent observed focus drifts when we measured the focus continuously. It shows that the major properties can be reproduced. For the field tilt parameters, we see the characteristic, non-physical anti-correlation of Stimulus Telescope parameters and Instrument parameters. Still, the field curvature parameters are not biased

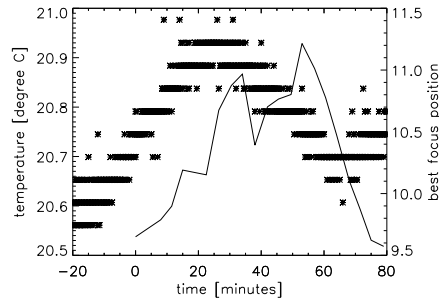


**Figure 9.** The stars represent the measured air temperature during a continuous focus measurement, and the line shows the measured focus. The focus follows the temperature with a time lag of 18 minutes.

if the measurements are started at a random time, and therefore their average value provides an estimate for the actual tilt.

We observed that the coefficients for the front and side camera are strongly correlated. This suggests that jitter or air currents, which act on the short time lag between the cameras and would destroy the correlation, play a minor role in the observed variation in the field tilt parameters. Table 2 gives the mean value and standard deviation of the 12 consecutive measurements.

Figure 11 shows all the field curvature measurements we obtained at the different test facilities. While the temperature fluctuations at GSFC caused large fluctuations of the measured values, the environments at LMSAL and ASO were more stable, which resulted in more consistent values.

We conclude that the side camera has a vertical gradient in the best focus position with the top of the field being half a focus step lower than the bottom. The gradient observed for the front camera is not significantly different from zero. This suggests that the plane of the side camera CCD slightly deviates from vertical to the optical axis. The field curvature has increased initially, but has later settled at a value of 0.4 focus steps from center to edge.

## 8. Image Motion

There are several moving parts in the Instrument, which can potentially lead to image offsets. While they can be corrected before the observables are calculated, they need to be known precisely, because any error will lead to cross talks between the spatial domain and the wavelength domain. Both a-priori knowledge of shifts introduced by particular waveplates, and Sun center coordinates obtained fitting the solar limb in individual filtergrams provide information about the instrumental image motion.

There are six rotating waveplates and one rotating polarizer in the Instrument. Three of the waveplates and the rotating polarizer are used to tune the Michelson interferometers and the tunable Lyot filter, and three waveplates are used for the polarization selection. In the following, we call them  $P1 \dots P3$  (polarization

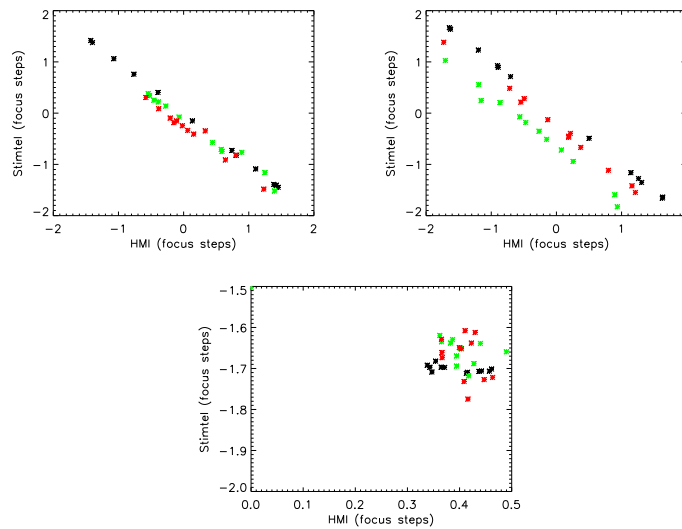


**Figure 10.** Horizontal (upper left) and vertical (upper right) field tilt as measured for the front camera (red) and the side camera (green), together with the result of the simulated measurements (black). The simulations enable us to explain the variations as an artifact of caused by an unstable outside temperature. The lower panel shows the quadratic term, which seems to have no strong sensitivity to the temperature drift.

selectors) and  $W1 \dots W4$  (wavelength selectors), in the order in which the light is passing through them (see Figure 1). All waveplates were separately rotated by 360 degrees in steps of 30 degrees. We determine the relative image shifts by cross correlating each image with a reference image. Figure 12 shows an example for the detected image motions.

The most striking feature is the vertical motion with an amplitude of about half a pixel which is produced by the two wavelength selector wave plates  $W2$  and  $W4$ , *i.e.* the waveplates tuning the two Michelson interferometers. We don't fully understand the reason why this vertical motion doesn't result in a phase shifted horizontal motion as would be suggested by a geometric distortion or a mounting error of the wave plates. However, the shift has been consistently seen on the ground, and it will be measured in space.

We note that while we detected a solid image shift with the rotating waveplates, the distortion introduced by the waveplates is generally only a few hundreds of a pixel. Occasionally observed shifts up to 0.1 pixel are not reproducible, and therefore are most likely thermally introduced distortions.

Other moving parts of the Instrument are the two focus wheels. Because some glass blocks are not perfectly mounted or show a wedge, they shift the image by several pixels. Figure 13 shows the offset as a function of the position of the focus wheels. Unlike the polarization and wavelength selector waveplates, the focus wheels don't move during regular observations. We note that focus sweep observation, which will be done regularly to determine the best focus position and the MTF, need to be performed with care because of the finite reaction time of the ISS to the image shifts introduced by the moving focus wheels.

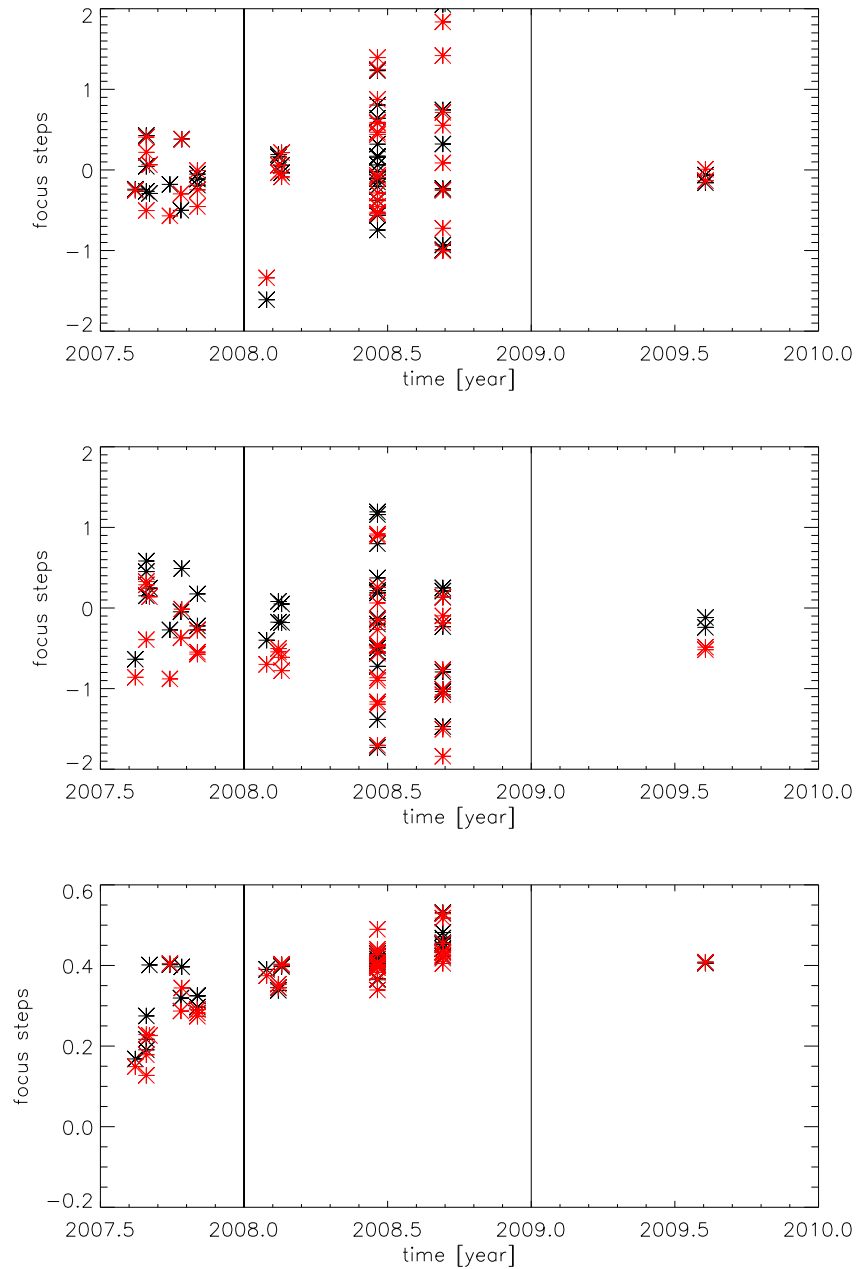


**Figure 11.** Measured value of the field tilt in horizontal (upper panel) and vertical (center panel) direction, and the quadratic field curvature (lower panel). The numbers represent the focus change in units of nominal focus steps from edge to edge for the focus gradient (left to right and bottom to top), and the change from center to edge for the quadratic focus term. The black stars show the data for the front camera, and the red stars show the data for the side camera. The horizontal axis represents the time of the measurement. The left section represents the field values obtained at LMSAL, the center section represents the values obtained at GSFC, and the right section represents the values obtained at ASO. At GSFC, temperature changes during the field curvature sequence (which take about one hour) introduce large fluctuations in the measured parameters, and only averages of large number of measurements are meaningful. The values measured at LMSAL and ASO suggest a field tilt of one half focus step in the vertical direction for the side camera. The field curvature, which can be measured even in unstable temperatures environment, has initially increased, but has stabilized later on.

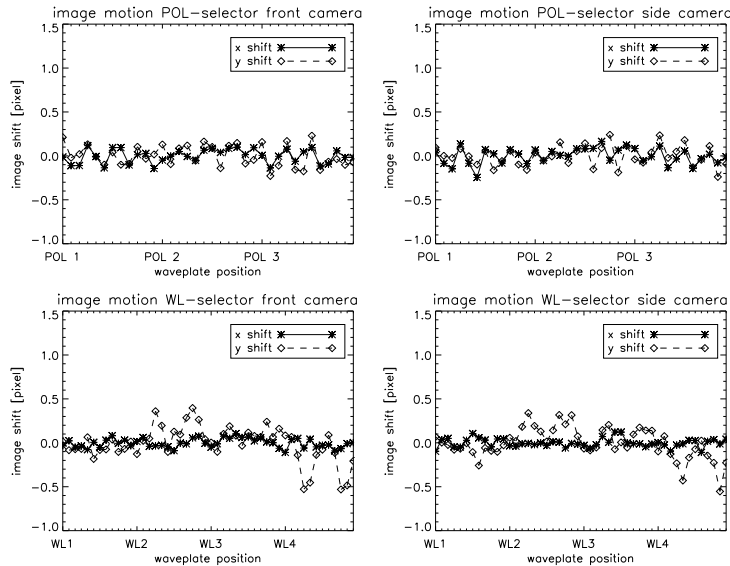


**Figure 12.** Image motion introduced by moving wave plates and polarizers. The left panels show the front camera, the right panels show the side camera.

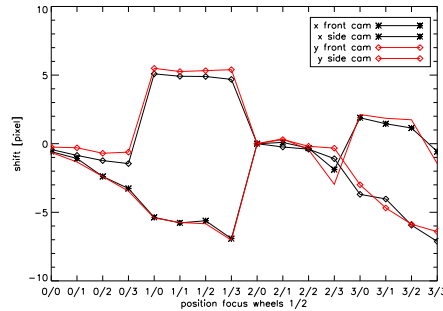


**Figure 13.** The image shifts introduced by the focus blocks. The labels on the horizontal axis show the thickness of the first and second glass plate in the optical path. The thickness is a multiple of 3.4 mm for the first focus wheel, and a multiple of 0.85 mm for the second focus wheel.

## 9. Flat Field

The flat field has been determined by the method presented in Kuhn, Lin, and Loranz (1991) and Toussaint, Harvey, and Toussaint (2003). Similar to the field curvature and distortion measurements, by offsetting the optical axis of the Stimulus Telescope and the Instrument, one can distinguish between the instrumental flat field and the inhomogeneous illumination from the Stimulus Telescope. We used a 27.4 mm diameter field stop target, which cuts off only the extreme edge of the field of view. It is large enough to not limit the field of view substantially, but still gives guidance about the relative displacement of Instrument and Stimulus Telescope. We note that because the illumination

varies only on large scales, the flatfield does not depend critically on an extremely accurate knowledge of the image offsets.

The resulting flat field (see Figure 14) shows the different gains of the four quadrants of the CCD. This is not a property of the CCD surface, but of their respective amplifiers. The small scale features of the flat field can be made visible by applying a high pass filter to the flat field (right panels). The circular structures show out-of-focus dust grains that are part of the optical flat field. The optical flat field is largely identical for both cameras, whereas the CCD flat fields are independent.

The flat field falls off sharply near the edge of the field of view. This is a result of vignetting caused by a manufacturing mistake resulting in an opening at the back-end of the Lyot filter, which is too small, and which is slightly obstructing the clear aperture of the Instrument. The unvignetted part of the optical field is large enough to always fully contain a properly centered solar image. The observables should therefore be unaffected by the vignetting.

There is a larger dust grain on the side camera CCD obscuring an area of about twelve pixels, (and several smaller ones on both cameras) reducing the intensity of several pixels below 50 % of the normal value. The signal in these pixels is too low to be simply corrected by applying the flat field. The affected pixels need to be treated as missing pixels and spatially interpolated.

We also discovered a stable horizontal structure with a period of  $128/3$ . The structure shows different strength for both CCD and for the different quadrants, but no apparent time variation.

As a measure of the large-scale flat field quality we look at the magnitude of the residuals. Figure 15 (right panel) shows the average residuals from the offset images. The images have been rebinned to reduce the photon noise. The residuals are probably caused by slight variations in the aperture illumination, which are ignored in the flat field derivation. The circular structures are residuals of dust grains in the Stimulus Telescope. The average residual inside the vignetting radius is 0.2%.

We noticed condensation on the CCD that produces geometric patterns when the Instrument is in the vacuum tank. Figure 14 shows how these patterns become stronger with time as long as the Instrument is in the vacuum tank. Images taken with the internal LED at GSFC show similar patterns. We expect the outgasing of the Instrument at the beginning of the mission to be so thorough that condensation doesn't become a problem during normal operations. In case contaminants should built up on the CCD, heaters can be switched on to clean up the CCD.

There are more stringent requirements on the small scale flat field, because it is critical to the sub-pixel spatial interpolation of the filtergrams. The accuracy must be better than 0.1% at any given time. Besides the above mentioned algorithm, small scale flat fields can be obtained from any low contrast image. The condensation patterns shown in Figure 14 lead to small-scale flat field changes on the entire CCD. Although the rate of the flat field changes depends strongly on the particular thermal environment of the Instrument, an order of magnitude estimate of the change may be derived from the fact that we saw a change of 0.2% in the area-average small scale flat field within a period of 5 weeks in which

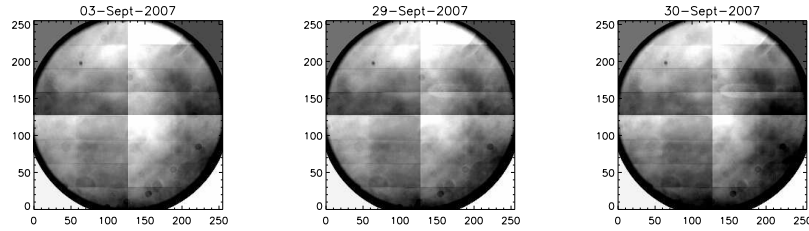


**Figure 14.** The three panels show the observed flat field in vacuum. The finger-like horizontal structure in the upper right quadrant becomes stronger with time. The color scale is saturated with a range from 0.95 to 1.05 for better visibility of the structure. Also, the quadrants have been corrected for the different quadrant gains.

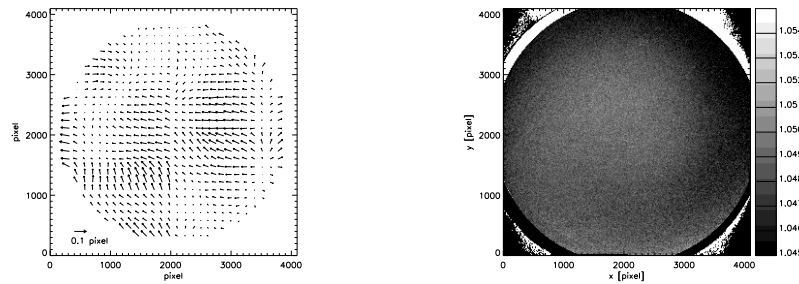


**Figure 15.** *Left panel:* Residual shifts between the images after removing a lateral shift, a rotation, and a fourth order polynomial for the mutual distortion. The spatial structure is dominated by the  $512 \times 2048$  pixel slabs of the CCD. *Right panel:* Averaged residuals from the offpoint flat field measurements. The residuals give an estimate of the error in the large scale variation of the flat field. The average error inside the vignetting radius is 0.2%.

the Instrument was kept in the vacuum tank. A mechanism to monitor the small scale flat field from regular filtergram observations at a temporal cadence of one day has been put in place to deal with any changes in the flat field (see Wachter and Schou (2009)). This way, we expect to achieve a flat field knowledge of better than 0.1% at any time.

## 10. Gain and Linearity

### 10.1. Camera Gain

The gain of the amplifiers of the four quadrants of the CCD is determined by varying the exposure time and determining the slope of the variance versus the signal. A number of exposures from 0 to 16 seconds were taken with the LED while the Instrument was in the vacuum tank. Figure 16 shows a plot of the average signal versus an estimate of the variance. The variance is estimated

**Table 3.** The inverse gain for the front and side camera obtained from a variation in exposure.

	front camera	side camera
lower left	15.91	15.83
lower right	15.91	16.27
upper left	16.27	16.10
upper right	15.45	16.92

from a pixel-by-pixel difference of two identical images. We see a clear linear dependence before saturation is reached at around 12000 DN. The variance drops after saturation, because electric charge is leaking to neighboring pixels. Figure 17 shows the inverse gain as a function of CCD position for the front and the side camera. As expected, the gain is different for each quadrant. The variation within the quadrant is probably a residual effect from the very inhomogeneous illumination of the CCD, which results in a different weight across the intensity range. The average gain for each quadrant is given in Table 3.

## 10.2. Linearity

Another important aspect of the CCD and camera performance is the linearity of the amplifiers. The linearity can be derived from the same data set as the gain. The center four pixels in a 64x64 rebinned imaged were fitted to a linear function of the exposure time (over the linear range) and the residuals plotted versus the intensity.

As can be seen from Figure 18 the intensities saturate at around 12000 DN for both cameras. At intensities below that the non-linearity is of the order 1%. The non-linearity is generally very repeatable but does show a weak temperature dependence.

## 11. Combining the Cameras

Depending on the choice of frame list (see Couvidat *et al.* (2010) for a discussion of frame lists), it will be required to combine filtergrams from both cameras to produce a single observable. To avoid systematic errors from the procedures, an accurate knowledge and a high degree of stability for the shifts between the two cameras is required. Moreover, we need to know the flat fields of both cameras, and their Modulation Transfer Functions.

The alignment of the cameras and their relative distortion can be measured by cross-correlating images. We measured the relative distortion and alignment with the random dot target and fitted a forth order polynomial to fit the relative distortion. Doing so, we obtain a residual distortion with a magnitude of a few hundredths of a pixel, which reflects the structure of the CCD (see Figure 15, left panel). The obvious cause for this pattern are small inhomogeneities in the lattice of CCD pixels. This structure is stable and can be modeled if necessary. Residual

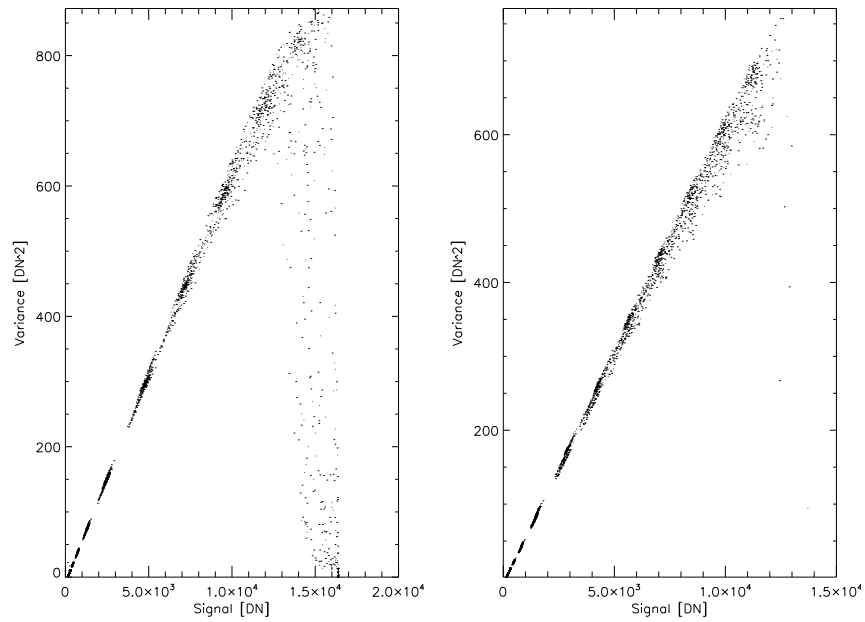


**Figure 16.** The variance as a function of signal intensity for front (left) and side (right) camera. The slope of this curve in the linear range is the gain of the camera amplifiers.

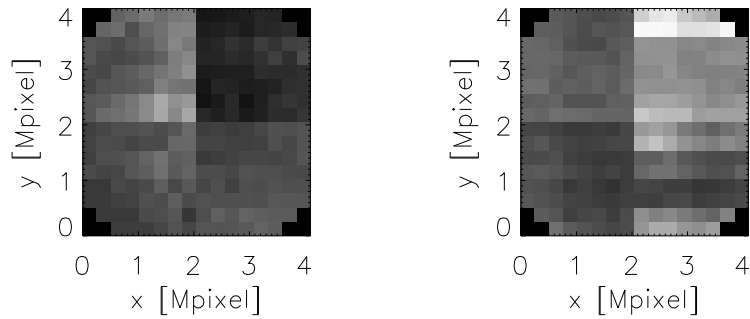


**Figure 17.** Inverse gain as a function of field position. The gray scale ranges from 15 through 18. The main signal comes from the four different amplifiers, the rest is due to inhomogeneities in the CCD.

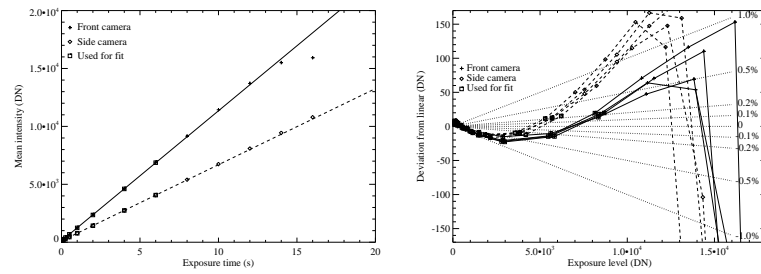


**Figure 18.** *Left panel:* Intensity as a function of exposure time for the front and the side camera. Only exposure times far away from the saturation level are used for the linear fit. *Right panel:* Residuals from a linear fit of the CCD intensity to the exposure time plotted versus intensity. The four curves for each camera show the results for the 4 pixels closest to the center of the CCD in 64x64 rebinned images (i. e. one per quadrant). The fits are in all cases done over the same set of exposure times.

errors have a random, time varying structure and are probably introduced by thermal fluctuations. They are of the order of a few hundredths of a pixel.

While the accuracy of the large scale flat field we obtain from the offpointing method for each individual camera is not sufficient to combine the cameras, we can very accurately determine the relative flat field from any image that is nearly simultaneously recorded in both cameras. The ratio of those images readily provides the relative flat field.

As shown in Chapter 3, we could not reliably measure any significant difference between the best-focus MTF of both cameras on the ground. However, we know that the best focus of the cameras differs by 0.2 focus steps, which leads to small differences in the MTF. As the main cause of uncertainty are the air currents, we may be able to find differences in the relative MTF and correct for them once we get data from space.

## 12. Conclusion

The Helioseismic and Magnetic Imager is a high precision monochromatic optical imager. The on-ground optical calibration shows that HMI meets all performance requirements, and guarantees our ability to produce observables of high enough quality to reach the HMI science goals. It also gives a clear guideline for the in-orbit calibration.

HMI is expected to achieve a Strehl ratio of 0.8 or better. The distortion of up to two pixels at the edge of the field of view has been determined with an accuracy of 0.05 pixels. The large scale flat field can be determined with an accuracy of 0.2% and for the small scale flat field we confirmed that knowing the flatfield in space at any time with an accuracy of 0.1 % or better is realistic. The Instrument focus varies from center-to-edge by 0.4 mm, and from edge to edge by less than 0.5 mm. The best focus is in the middle of the adjustable focus range, and the offset and rotation of the two cameras has been determined to fractions of a pixel.

Modeling helped to understand the behavior of the Instrument in a sometimes unstable temperature environment, and to make sure the Instrument will meet the specifications when operated in space. The continuous monitoring of the Instrument's performance during a time period of more than two years makes us confident that HMI will provide data of outstanding quality during its mission.

**Acknowledgements** This work has been supported by the NASA grant NAS5-02139 (HMI). Many people were involved in the calibration efforts for the instrument. We thank staff members at LMSAL, GSC, and ASO for their support. In particular we thank Dave Kirkpatrick, Darrel Torgerson, Bob Stern, and Brett Allard. We also thank Phil Scherrer, Ted Tarbell, and Alan Title for their input.

## References

- Bray R.J., Loughhead R.E.: 1979, Sunspots..
- Couvidat S., Schou J., Schine R.A., Scherrer P.H., Bush R.I.: 2010, Wavelength Dependence of the Helioseismic and Magnetic Imager Instrument. *Solar Phys.*
- Couvidat S., Zhao J., Birch A.C., Kosovichev A.G., Duvall T.L. Jr., Parchevsky K., Scherrer P.H.: 2010, Implementation and Comparison of Acoustic Travel-Time Measurement Procedures for the Helioseismic and Magnetic Imager Time-Distance Helioseismology Pipeline. *Solar Phys.*
- Jefferies, S.M., Duvall, T.L. Jr.: 1991, A simple method for correcting spatially resolved solar intensity oscillation observations for variations in scattered light. *Solar Phys.* **132**, 215–222. doi:10.1007/BF00152283.
- Kuhn, J.R., Lin, H., Loran, D.: 1991, Gain calibrating nonuniform image-array data using only the image data. *Pub. Astron. Soc. Pac.* **103**, 1097–1108.
- Pierce, A.K., Slaughter, C.D.: 1977, Solar limb darkening. I - At wavelengths of 3033-7297. *Solar Phys.* **51**, 25–41. doi:10.1007/BF00240442.
- Scherrer, P.H., Bogart, R.S., Bush, R.I., Hoeksema, J.T., Kosovichev, A.G., Schou, J., Rosenberg, W., Springer, L., Tarbell, T.D., Title, A., Wolfson, C.J., Zayer, I., MDI Engineering Team, : 1995, The Solar Oscillations Investigation - Michelson Doppler Imager. *Solar Phys.* **162**, 129–188.
- Schou J., Scherrer P.H., Wachter R., Bush R.I., Couvidat S.: 2010, The Helioseismic and Magnetic Imager Design and Calibration. *Solar Phys.*
- Toner, C.G., Jefferies, S.M., Duvall, T.L. Jr.: 1997, Restoration of Long-Exposure Full-Disk Solar Intensity Images. *Astrophys. J.* **478**, 817–+. doi:10.1086/303836.
- Toussaint, R.M., Harvey, J.W., Toussaint, D.: 2003, Improved Convergence for CCD Gain Calibration Using Simultaneous-Overrelaxation Techniques. *Astronom. J.* **126**, 1112–1118. doi:10.1086/376846.
- Wachter, R., Schou, J.: 2009, Inferring Small-Scale Flatfields from Solar Rotation. *Solar Phys.* **258**, 331–341. doi:10.1007/s11207-009-9406-x.